Energy & Environmental Science

ROYAL SOCIETY OF CHEMISTRY

PAPER

View Article Online
View Journal | View Issue

Cite this: *Energy Environ. Sci.*, 2025, **18**, 4787

Deciphering the interplay between tin vacancies and free carriers in the ion transport of tin-based perovskites†

Luis Huerta Hernandez,[a] Luis Lanzetta,[a] Anna M. Kotowska,[b] Ilhan Yavuz,[c] Nikhil Kalasariya,[d] Badri Vishal,[a] Marti Gibert-Roca,[a] Matthew Piggott,[b] David J. Scurr,[b] Stefaan De Wolf,[a] Martin Stolterfoht[d] and Derya Baran*[a]

Mixed ionic-electronic conduction is a prevalent phenomenon in metal halide perovskites, having a critical impact in multiple optoelectronic applications. In Sn-based halide perovskites, their higher hole density ([*p*]) owing to the facile formation of Sn vacancies (V_{Sn}^{2-}) induces substantial electronic transport differences *versus* their Pb-based analogues. However, the influence of [*p*] and V_{Sn}^{2-} on their ionic transport properties remains elusive. Herein, the link between electronic and ionic transport is unravelled in a compendium of Sn-based perovskite compositions. Specifically, ionic and electronic conductivities are found to concomitantly rise with higher Sn content. Using a combination of electrical characterization techniques, a rise in [*p*] and V_{Sn}^{2-} is demonstrated to increase mobile ion density, enhancing lateral ion migration and ionic conductivity. First-principles simulations reveal that [*p*] and V_{Sn}^{2-} jointly lower the energy barrier for iodide migration from 0.38 eV to 0.12 eV. Chemical mapping techniques support these observations by identifying the bias-induced migration of iodide and formamidinium ions in compositions with higher [*p*] and V_{Sn}^{2-}. These fundamental insights on the ionic-electronic coupling will enable next-generation of Sn-based perovskite technologies with improved performance and stability.

Received 3rd February 2025,
Accepted 10th April 2025

DOI: 10.1039/d5ee00632e

rsc.li/ees

Broader context

Halide perovskites based on tin-lead mixtures offer unique infrared absorption properties that enable efficient all-perovskite tandem solar cells, an emerging photovoltaic technology combining affordability and high energy output. However, the low stability of these materials continues to hinder their progress towards practical applications. A key phenomenon that limits solar cell lifetime is the migration of constituent ions within the perovskite layer. Hence, understanding the fundamental mechanisms governing ion transport in halide perovskites is paramount to design more stable perovskite photovoltaics. While ion migration in lead-based perovskite has received extensive attention, the study of this process in tin-based analogues remains at its early stages. In this work, we employ a comprehensive set of characterization techniques and first-principles simulations to unveil the mixed ionic-electronic transport mechanism in a wide compositional range of tin-based perovskites. We demonstrate that ionic transport in these materials is governed by the combined effect of tin vacancies and electronic hole carriers in the perovskite. These crucial insights will not only inspire novel design rules for stable tin-based perovskite solar cells, but also for related optoelectronic applications beyond photovoltaics.

Introduction

Metal halide perovskites, represented by the ABX_3 formula (A = methylammonium (MA^+), formamidinium (FA^+), and/or Cs^+; B = Pb^{2+} and/or Sn^{2+}; X = I^-, Br^- and/or Cl^-), are promising semiconductors for a myriad of optoelectronic applications. The combination of their remarkable optical properties and their low formation energies result in high performance optoelectronic devices compatible with low-cost fabrication methods.[1] However, the relatively soft crystal lattice allows halide ions to easily propagate under operational conditions,

[a] *Materials Science and Engineering Program (MSE), Physical Sciences and Engineering Division (PSE), King Abdullah University of Science and Technology (KAUST), Thuwal 23955-6900, Saudi Arabia. E-mail: derya.baran@kaust.edu.sa*
[b] *Advanced Materials and Healthcare Technologies, School of Pharmacy, University of Nottingham, NG7 2RD, UK*
[c] *Marmara University, Physics Department, 34722 Kadikoy, Istanbul, Turkey*
[d] *Electronic Engineering Department, The Chinese University of Hong Kong, Sha Tin N.T., Hong Kong SAR, China*

† Electronic supplementary information (ESI) available. See DOI: https://doi.org/10.1039/d5ee00632e

such as high temperature, illumination, or electrical bias.[2,3] The migration of halide ions as vacancies or interstitials strongly influences the charge transport properties of perovskites, as evidenced by their high ionic conductivity (σ_{ion}) and mobile ion density (n_{ion}) relative to their electronic conductivity (σ_{elec}) and charge carrier concentration, respectively.[4–6] The mixed ionic-electronic conduction results in several unusual phenomena observed in perovskite devices, including hysteresis in current–voltage (*IV*) curves, transient responses to external stimuli, formation of charge extraction barriers at interfaces with contacts, and detrimental chemical reactions between mobile ions and contacts.[7–12]

A critical aspect determining the mixed conduction properties of halide perovskites is their composition.[5,9,13] Particularly, the partial or complete substitution of Pb^{2+} by Sn^{2+} at the perovskite B-site induces a dramatic increase in the hole carrier concentration [*p*].[14–20] Interestingly, the ion transport properties of Sn-based perovskites exhibit marked differences compared to their Pb counterparts. For instance, the phenomenon of halide segregation, where mixed iodide/bromide (I^-/Br^-) compositions separate into individual I^--rich and Br^--rich domains under illumination, is not observed in Sn-based perovskites compared to Pb analogues.[21–23] Moreover, solar cells and field effect transistors fabricated from mixed Sn–Pb perovskites present suppressed hysteresis regardless of the voltage scan rate.[24,25] While these reports suggest that ion transport is reduced by the incorporation of Sn^{2+}, several other studies have highlighted the substantial role of mobile ions in the degradation and performance of Sn-based perovskite solar cells. Specifically, short-circuit current density (J_{sc}) losses in mixed Sn–Pb perovskite solar cells have been attributed to a screening of the built-in potential caused by a high mobile ion density ($n_{ion} \sim 10^{17}$ cm^{-3}).[8] Furthermore, mobile ion-induced hysteresis has been correlated to lower efficiency and reduced stability.[26,27] Photo-induced iodide vacancies (V_I^+) and iodide interstitials (I_i^-) are suggested to initiate the oxidation of I^- to molecular iodine (I_2), which in turn can detrimentally promote further Sn oxidation.[28–31] Importantly, the majority of these reports investigate ion migration through indirect and/or qualitative methods (*i.e.*, time-dependent photoluminescence mapping or hysteresis analysis in *IV* curves), while focusing on a limited number of Sn-based perovskite compositions. Therefore, a systematic quantification of ion transport properties considering the distinct defect chemistry of Sn-based perovskites in a comprehensive compositional space is yet lacking.

The defect chemistry of Sn-based perovskites is significantly influenced by Sn vacancies (V_{Sn}^{2-}), which result from the facile oxidation of Sn^{2+} to Sn^{4+} and are therefore prevalent.[17] Moreover, V_{Sn}^{2-} are known to act as acceptor defects that increase [*p*].[18,32] Considering the mixed ionic-electronic character of halide perovskites, we anticipate that formation of V_{Sn}^{2-} and the consequent increase in [*p*] may impact the ion transport properties. Revealing this link could unfold overlooked transport phenomena in Sn-based perovskites.

In this work, we quantify the ionic-electronic transport properties for a broad selection of Sn-based perovskite compositions ($ASn_xPb_{1-x}I_3$, where A = MA^+, FA^+, and $Cs_{0.15}FA_{0.85}$ and x = 0, 0.25, 0.5, 0.75 and 1). Our findings show that regardless of the A-site composition, the σ_{ion} and σ_{elec} concomitantly increase as the Sn fraction rises. By tuning [*p*] and V_{Sn}^{2-} in mixed Sn–Pb perovskites with the additive SnF_2, we discover that the increase in the σ_{ion} and mobile ion density (n_{ion}) correlates with the formation of V_{Sn}^{2-} and the consequent rise in [*p*]. Utilizing multiple chemical mapping techniques, we identify that lateral bias-induced migration of I^- and FA^+ is promoted in samples with higher V_{Sn}^{2-} and [*p*]. First-principles calculations reveal that the simultaneous presence of hole charge carriers and V_{Sn}^{2-} reduce the activation energy barrier of I^- migration from 0.38 eV to 0.12 eV. These results reveal that ion transport in Sn-based perovskites is strongly influenced by the joint effect of V_{Sn}^{2-} and hole carriers, which is a critical aspect of the mixed ionic-electronic transport mechanism in this class of materials. The joint effect of V_{Sn}^{2-} and hole carriers on ion transport presented herein describe a central aspect of the mixed ionic-electronic transport in these materials, enabling the design of robust Sn-based perovskite optoelectronics.

Results and discussion

Ionic and electronic conductivities of Sn-based perovskites

To understand how the Sn content influences the ionic transport properties of $ASn_xPb_{1-x}I_3$ perovskites (where A = MA, FA or $Cs_{0.15}FA_{0.85}$; we test this last composition due to its relevancy to solar cells and transistors),[24,25] we perform galvanostatic polarization measurements on devices with coplanar contacts under N_2 atmosphere and dark conditions (device architecture: Au/Cr/$ASn_xPb_{1-x}I_3$/Cr/Au; channel width: 150 μm). A schematic of the device is shown in Fig. 1a (inset), and fabrication details are provided in the Experimental section. Galvanostatic polarization has been widely exploited to quantify the σ_{ion} and σ_{elec} of several Pb perovskites.[4,5,33–35] The measurement consists of tracking voltage changes through time while applying a constant electrical current (Fig. 1a). Initially, mobile ions and electrons begin to flow, both contributing to the total conductivity of the system ($\sigma_{tot} = \sigma_{ion} + \sigma_{elec}$). This defines a starting voltage V ($t \approx 0$), which is used to estimate σ_{tot}. Since ions cannot be extracted through the ion-blocking contacts, these will progressively accumulate at the interface with the electrodes. The depletion of mobile ions will cause a decrease in σ_{ion} (and thus a drop in σ_{tot}), resulting in a voltage surge, a consequence of Ohm's law. At $t = a$, all mobile ions are depleted, and the voltage signal stabilizes at a constant value $V(t = a)$, indicating that the flowing current is now constituted only of electronic carriers. From $V(t = a)$, σ_{elec} is calculated and therefore, σ_{ion} can be inferred. Further details on the measurement assumptions, the effect of electrode metals (Fig. S1–S3, ESI†), and the duration of the galvanostatic polarization measurement (Fig. S4, ESI†) are provided in Note S1 (ESI†).

Fig. 1b shows the galvanostatic polarization curves of $FASn_xPb_{1-x}I_3$ (x = 0, 0.25, 0.5, 0.75, and 1). We found that all

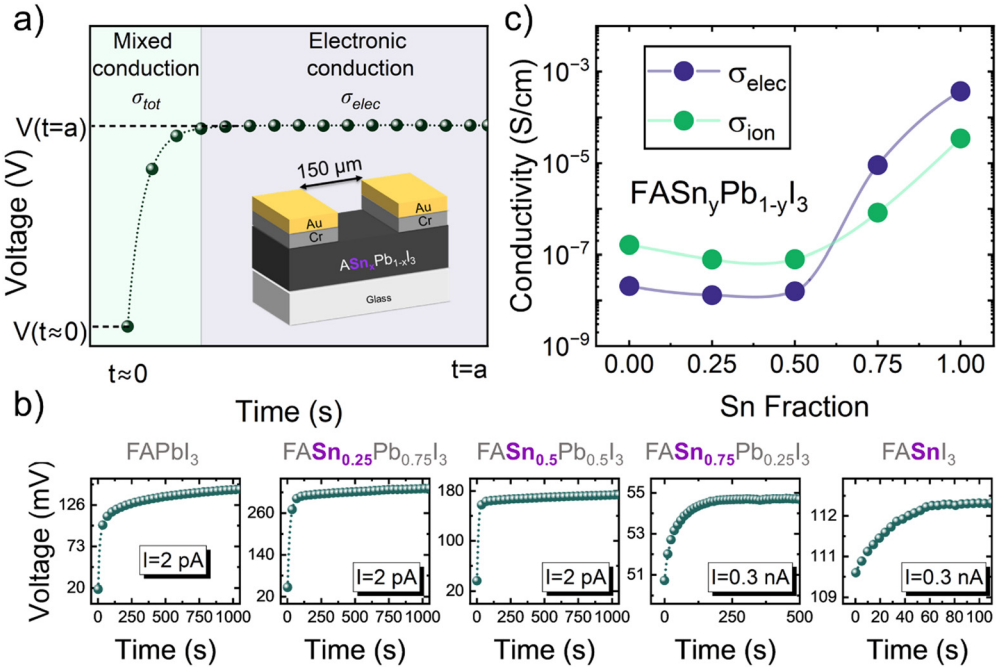

Fig. 1 (a) Schematic of a typical polarization curve from a mixed ionic-electronic conductor. The inset shows the device architecture used in these experiments. The calculation of σ_{ion} is derived from $\sigma_{ion} = \sigma_{tot} - \sigma_{elec}$ (b) galvanostatic polarization curves of $FASn_xPb_{1-x}I_3$ (x = 0.0, 0.25, 0.50, 0.75 and 1), the electrical current used for the measurement varied according to the σ_{tot} of each composition. (c) σ_{elec} and σ_{ion} as a function of Sn fraction for $FASn_xPb_{1-x}I_3$ samples.

samples exhibited mixed conduction behavior regardless of the Sn content. This observation was further confirmed for different A-site compositions such as $MASn_yPb_{1-y}I_3$ (y = 0, 0.25, 0.5, and 0.75; Fig. S5a, ESI†) and $Cs_{0.15}FA_{0.85}Sn_zPb_{1-z}I_3$ (z = 0, 0.5, and 1; Fig. S6a, ESI†), indicating that mixed conduction prevails irrespectively of the A-cation selection in Sn-based perovskites. From the curves in Fig. 1b, we extracted σ_{ion} and σ_{elec} of FA-based perovskites as shown in Fig. 1c (σ_{ion} and σ_{elec}, trends for MA- and $Cs_{0.15}FA_{0.85}$-based perovskites presented in Fig. S5b and S6b, ESI†). In agreement with previous reports, we detect an increase in σ_{elec} with higher Sn content (x, y, $z > 0.5$) for all the A-site compositions studied. In $FASn_xPb_{1-x}I_3$, σ_{elec} increases approximately four orders of magnitude, spanning from 2.07×10^{-8} S cm^{-1} in $FAPbI_3$ to 3.73×10^{-4} S cm^{-1} in $FASnI_3$ (a full list of values is provided in Table S1, ESI†). We mainly attribute the observed trend in σ_{elec} to the higher density of V_{Sn}^{2-} at larger Sn fractions and thus an increase in the $[p]$.[14,16,17] Additional factors that may play a minor role on the observed σ_{elec} trend (*i.e.*, bandgap narrowing) are discussed in Note S2 (ESI†).

Intriguingly, in the FA-series (Fig. 1c), σ_{ion} increases up to 2 orders of magnitude (from 1.64×10^{-7} S cm^{-1} to 2.07×10^{-5} S cm^{-1}) when transitioning from the Sn-lean ($x \leq 0.5$) to the Sn-rich compositions ($x \geq 0.75$). We notice a similar trend for the MA- and $Cs_{0.15}FA_{0.85}$-compositions (Fig. S5 and S6, respectively, ESI†). Specifically, we observe that (i) σ_{ion} is higher than σ_{elec} for Sn-lean compositions, and that (ii) σ_{elec} dominates the σ_{tot} relative to σ_{ion} for Sn-rich compositions. By considering the significant $[p]$ found in Sn-rich samples and that holes are more mobile than ions,[36,37] it is reasonable to expect that σ_{elec} exceeds σ_{ion} in these compositions. However, the higher σ_{elec} compared to σ_{ion} does not infer that ion migration is reduced. Instead, it is apparent in Fig. 1c that σ_{elec} and σ_{ion} are coupled as both rise when the Sn content increases. Based on the magnitude of σ_{ion}, these results indicate that significant ion migration is happening in Sn-based perovskites, implying substantial ionic-electronic conduction in these materials.

Mixed ionic-electronic transport in Sn-based perovskites

To understand why σ_{ion} is enhanced at higher Sn : Pb ratios, we initially consider how the Sn content regulates the grain size and crystallinity. Earlier reports on Pb perovskites show that higher lattice strain and smaller grain size (*i.e.*, larger density of grain boundaries) correlate to a reduced activation energy for I^- migration.[38–41] Notably, both of these parameters are heavily influenced by the addition of Sn, as faster crystallization rates are usually observed.[42,43] For the majority of the A-site compositions, top-view scanning electron microscopy (SEM) images reveal larger grain sizes at higher Sn fractions (Fig. S7 and S8, ESI†). However, in pure Sn-based compositions ($FASnI_3$, $MASnI_3$, and $Cs_{0.15}FA_{0.85}SnI_3$) we identify the formation of pinholes, which further increase the grain boundaries density and hence, the possible ion migration pathways.[40] X-Ray diffraction (XRD) patterns from several compositions ($FASn_xPb_{1-x}I_3$ being the exception) present a higher intensity of the characteristic perovskite diffraction peak at ~14° as the Sn content increases, suggesting enhanced crystallinity (Fig. S9, ESI†). Furthermore, we record a shift to larger 2θ values with

added Sn in the lattice, suggesting a lattice contraction due to the smaller radius of Sn^{2+} compared to Pb^{2+} (Fig. S10a–c, ESI†).[44] We further investigate XRD peak broadening by measuring their full width at half maximum (FWHM). Our results indicated that the FWHM follows an overall decreasing trend as the Sn content increases (Fig. S10d–f, ESI†). Lower FWHM values have been interpreted as evidence of reduced microstrain.[45,46] Taken together, the alterations in morphology and crystallinity resulting from the substitution of Sn do not reveal any clear trends behind the observed high σ_{ion}.

Given the non-obvious relationship between σ_{ion} and microstructure in our samples, we sought to adjust $[p]$ and V_{Sn}^{2-} density (since these variables also correlates with increasing Sn content) without significantly altering the morphology and crystallinity. For this, we fixed the composition to $FASn_{0.5}Pb_{0.5}I_3$ while varying the concentration of SnF_2 (0, 2.5, 5, and 10 mol% respect to the SnI_2 concentration). This additive has played a pivotal role in the development of state-of-the-art Sn-based perovskite devices.[47,48] SnF_2 lessens $[p]$ by capturing Sn^{4+} impurities and reducing the formation of V_{Sn}^{2-}, in Note S3 (ESI†) we explain in more detail the working mechanism of SnF_2.[49–51] Consistent with previous reports, we find that changes in average grain size, crystallinity and FWHM upon addition of SnF_2 are much smaller compared to those observed with variations of Sn content (Fig. S11 and S12, ESI†).[50,52]

Fig. 2a shows the galvanostatic polarization curves of the SnF_2 containing samples. As the SnF_2 concentration increases, we observe a reduction in σ_{elec} and σ_{ion} (Fig. 2b). After 5 mol% SnF_2, σ_{elec} and σ_{ion} present no significant changes. Since $\sigma_{elec} = q[p]\mu_h$ (where q is the elementary charge and μ_h represents the hole mobility), a lower σ_{elec} due to $[p]$ compensation by SnF_2 is consistent. We do not anticipate that variations in μ_h influence σ_{elec}, as μ_h is known to remain relatively constant across different SnF_2 concentrations.[50] Therefore, the reduction of σ_{ion} appears to be coupled to the depletion of $[p]$ and V_{Sn}^{2-}, as these are the variables that are expected to change the most upon SnF_2 addition.

Analogous to σ_{elec}, the σ_{ion} from a particular ionic species is derived from its charge (z), the mobile ion mobility (μ_{ion}), and n_{ion} ($\sigma_{ion} = z\mu_{ion}n_{ion}$).[53] If a relationship exists between $[p]$ (and consequently V_{Sn}^{2-}) and σ_{ion} upon SnF_2 addition, then a coupling between $[p]$ and n_{ion} is plausible. It is also possible that $[p]$ influences μ_{ion}; a more in-depth discussion is provided in Note S4 and Fig. S13 (ESI†). To test if $[p]$ and n_{ion} are linked, we quantify both parameters as a function of SnF_2 concentration by performing Mott–Schottky (MS) analysis. This measurement records the depletion layer capacitance (C_{depl}) of semiconductor junctions as a function of an applied bias, where each potential is superimposed by an AC bias signal. The AC frequency determines what type of species (*i.e.*, ionic or electronic) creates the charge density profile that causes the fluctuations of the depletion layer width. At high frequencies (10^4–10^6 Hz), MS analysis can estimate carrier concentrations exceeding 10^{16} cm^{-3} for perovskite films with a thickness $\approx$300 nm.[54,55] According to values derived from Hall measurements in $MA_{0.6}FA_{0.4}Sn_{0.5}Pb_{0.5}I_3$ composition ($\approx 10^{17}$ cm^{-3}), high-frequency MS represents a suitable option to determine carrier concentration in Sn-rich compositions,[56] although we note, that the contribution of mobile ions to the high-frequency results (*e.g.* due to the much slower voltage sweep during the measurement) cannot be ruled out yet. More recently, it was demonstrated that the extraction of the n_{ion} can be performed at low frequencies ($\sim$1 Hz).[57] Assuming that one species is dominant (*e.g.* I^- or V_I^+), the low-frequency capacitance relates to the formation of a depletion layer due to the displacement of the dominant species (a more detailed explanation on the capacitance–voltage behavior in perovskites is found in Note S5, ESI†).

We extract n_{ion} and $[p]$ from the $FASn_{0.5}Pb_{0.5}I_3$ samples using the previously selected SnF_2 concentrations (details on sample preparation are provided in the Experimental section). In Fig. 3a, we show the low-frequency capacitance–voltage (C–V) data, where we set the AC signal to 4 Hz. From the linear dependency between C^{-2} and the voltage applied (V_{app}), n_{ion} is

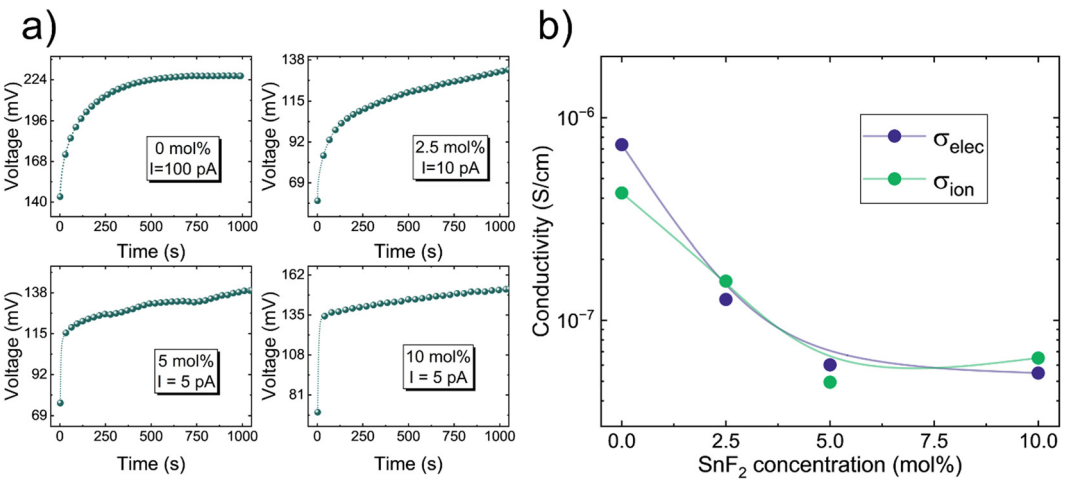

Fig. 2 (a) Galvanostatic polarization curves from $FASn_{0.5}Pb_{0.5}I_3$ samples with different SnF_2 concentrations: 0, 2.5, 5, and 10 mol% (b) σ_{elec} and σ_{ion} as a function of SnF_2 concentration.

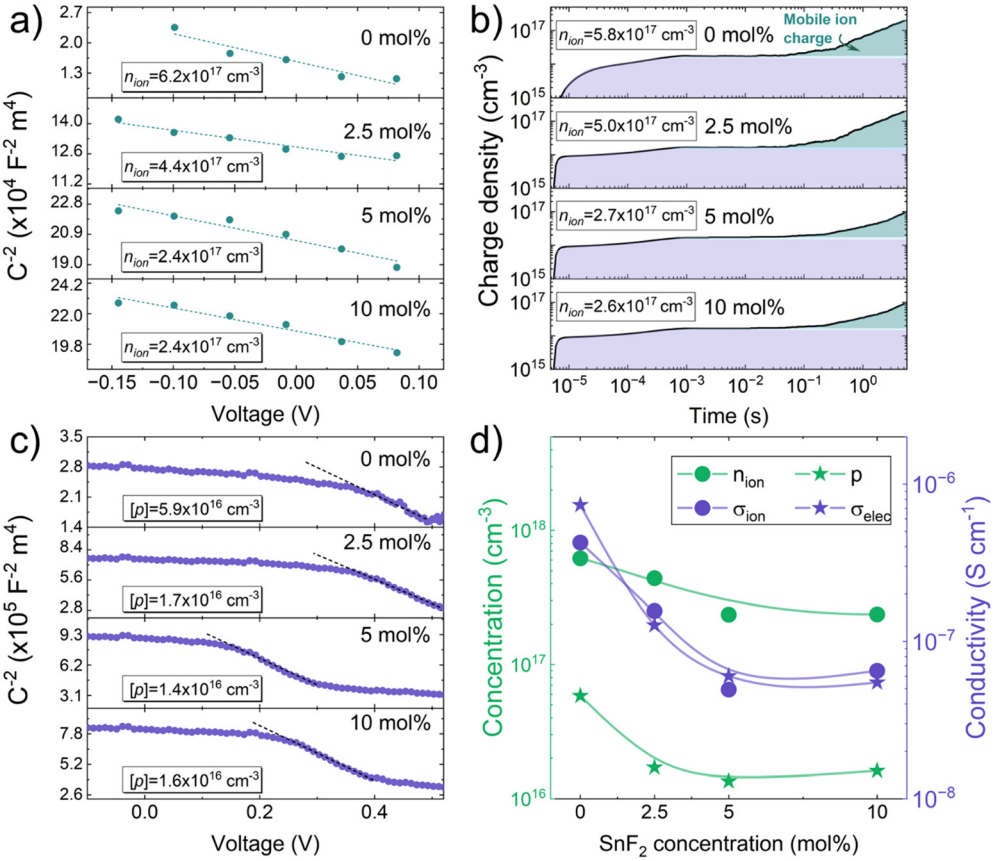

Fig. 3 (a) Low-frequency MS analysis; the AC frequency used is 4 Hz with an amplitude of 10 mV. (b) BACE measurements; the light purple, light blue, and light green-colored regions indicate the contribution from the electrode charge, the electronic charges that were injected at V_{oc}, and the mobile ions, respectively. These measurements were carried out with samples encapsulated with a UV-curated epoxy and dark conditions. (c) High-frequency MS analysis; the AC frequency used is 10 kHz with an amplitude of 10 mV. The samples fabricated for all of these measurements have the following architecture: ITO/PEDOT:PSS (30 nm)/$FASn_{0.5}Pb_{0.5}I_3$ (300 nm)/C_{60} (25 nm)/BCP (7 nm)/Cu (100 nm), where the selected SnF_2 concentrations are: 0, 2.5, 5, and 10 mol%. The capacitance–voltage measurements are carried under a N_2 environment and dark conditions. (c) n_{ion}, p, σ_{ion}, and σ_{elec} as a function of SnF_2 concentration in a $FASn_{0.5}Pb_{0.5}I_3$ perovskite. For this figure, σ_{ion}, and σ_{elec} were derived from the galvanostatic polarization measurements, n_{ion} values were selected from the low-frequency MS analysis, and p was obtained from the high-frequency MS analysis.

estimated from eqn (1):[57]

$$\frac{d\left(C_{depl}^{-2}\right)}{dV_{app}} = -\frac{2}{n_{ion} q \varepsilon \varepsilon_0} \quad (1)$$

where ε_0 is the vacuum permittivity and ε is the perovskite relative permittivity. Our results indicate that as the SnF_2 concentration increases from 0 to 10 mol%, the n_{ion} gradually reduces from 6.2×10^{17} to 2.4×10^{17} cm^{-3}. To corroborate the obtained C–V values of n_{ion}, we conduct bias assisted charge extraction (BACE) measurements. BACE records the temporal evolution of charge density upon switching from open-circuit voltage (V_{oc}) to 0 V.[8] Fig. 3b illustrates the charge density progression, which reveals two distinct features. The initial increase at $\approx 10^{-6}$ s corresponds to a combination of the injected or doping-induced electronic carriers and the electrode charge. The subsequent rise at $\approx 10^{-1}$ s is associated with the contribution of the mobile ions. The BACE-derived values exhibit n_{ion} decreasing from 5.8×10^{17} to 2.6×10^{17} cm^{-3} as the SnF_2 concentration increases. Although, a complete saturation of the transient was not observed, meaning that n_{ion} could be underestimated. The magnitudes of the n_{ion} from the BACE measurements are thus in excellent agreement with the low-frequency C–V experiments and in line with previously reported values.[8]

Fig. 3c displays the high-frequency C–V measurements of the same compositions (acquired at 10 kHz). MS analysis shows that $[p]$ drops from 5.85×10^{16} to 1.6×10^{16} cm^{-3} when the SnF_2 concentration increases from 0 to 10 mol%. In Fig. 3d, we converge all the transport measurements performed (n_{ion}, σ_{ion}, $[p]$, and σ_{elec}) as a function of the SnF_2 concentration. Our findings indicate that the reduction of σ_{ion} and σ_{elec} upon SnF_2 addition is caused by the corresponding decrease of n_{ion} and $[p]$, respectively. This strongly suggests the formation of V_{Sn}^{2-}, and the resulting increase in $[p]$, modulate the ionic transport in Sn-based perovskites.

Atomistic insights on mixed ionic-electronic transport

In Sn-based perovskites, the modulation of $[p]$ and n_{ion} by tuning SnF_2 concentration is inherently linked to a change of V_{Sn}^{2-} density. Hence, it is important to consider how both the

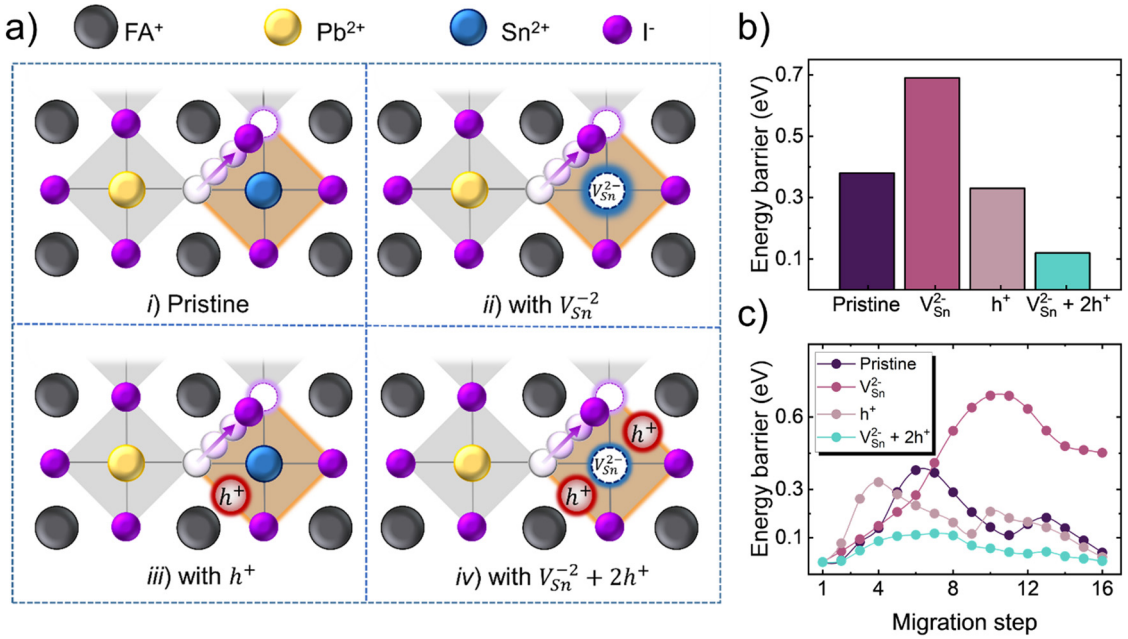

Fig. 4 (a) Theoretical model of the iodide migration pathway in a $FAPb_{0.5}Sn_{0.5}I_3$ lattice under four scenarios: (i) V_I^+ (*i.e.* the pristine case), (ii) V_I^+ and V_{Sn}^{2-}, (iii) V_I^+ and h^+, and (iv) V_I^+, V_{Sn}^{2-}, and $2h^+$. (b) The energy barriers for iodide migration of each proposed scenario. (c) Relative energy landscapes of the system during iodide migration, the *x*-axis represents the iodide migration step during its transition towards an adjacent V_I^+.

absence of Sn^{2+} in the lattice and the consequent increase in electronic charge carriers influence the possible ion migration pathways at the atomic scale. To this end, we perform density functional theory (DFT) simulations on $FAPb_{0.5}Sn_{0.5}I_3$ to study the influence of V_{Sn}^{2-}, holes (h^+), and their combined effect on the energy barrier of I^- migration (computational details are provided in the Experimental section). We calculate the I^- migration energy barriers in the presence of the following defects in the lattice: (i) V_I^+ (*i.e.*, the pristine case), (ii) V_I^+ and V_{Sn}^{2-}, (iii) V_I^+ and h^+, and (iv) V_I^+, V_{Sn}^{2-}, and $2h^+$ (Fig. 4a). DFT calculations predict an energy barrier of 0.38 eV for the pristine case (Fig. 4b). This value is closely aligned with previously reported energy barriers in Pb perovskites,[58] suggesting that Sn^{2+} ions do not significantly alter the I^- migration dynamics. In contrast, the introduction of V_{Sn}^{2-} increases the barrier up to 0.69 eV. This is in agreement with previous reports and has been attributed to a substantial rearrangement of the lattice structure caused by the V_{Sn}^{2-}.[25] Nonetheless, the energy barrier is reduced to 0.33 eV when we consider the effect of h^+ in the calculations. The barrier drops even further to 0.12 eV when $2h^+$ and V_{Sn}^{2-} are involved. Given the p-type character of Sn-based perovskites, we propose that excess of h^+ will likely remain localized near the V_{Sn}^{2-} vicinity.[59] The positive charge of h^+ could facilitate the migration of the negatively charged I^- due to attractive electrostatic interactions, shortening the migration pathway (Fig. 4c).

Furthermore, to elucidate the effect of spatial inhomogeneity (regular features in real polycrystalline films) it is important to consider how other defects beyond V_{Sn}^{2-} influence the energy barrier for I^- migration (Fig. S15, ESI†). We find that I^- and Sn^{2+} interstitial defects (I_{int} and Sn_{int}, respectively) raise the energy barrier above 1 eV, with a highest energy barrier achieved with I_{int}. Alternatively, I^- on Sn^{2+} sites (I_{Sn}) and Sn^{2+} on I^- sites (Sn_I) defects present energy barriers below 1 eV, where Sn_I defects show particularly low energy barriers of 0.36 eV. These results suggest that regions where I^- poor conditions exist (*i.e.* regions where I_i is less likely to form but more likely to develop Sn_I defects) could similarly facilitate I^- migration. Additionally, we also evaluate the effect of the surface (*i.e.*, crystal termination such as that potentially found on grain boundary or pinhole) on the formation of several defects by calculating the difference between the defect formation energy in the bulk and on the surface ($\Delta\Delta H = \Delta H_{bulk} - \Delta H_{surf}$) (Fig. S16, ESI†). The $\Delta\Delta H$ of V_I and V_{Sn}, the defects associated with I^- mobility in our calculations, are notably the lowest; suggesting that formation of such defects is potentially favorable in the bulk and surface. While we acknowledge that sample heterogeneity has a significant impact on the ion transport dynamics, the results presented herein emphasize the role of V_{Sn} and h^+ in the I^- migration in Sn-based perovskites, which is in good agreement with the experimental observations.

Visualizing ion migration

To visualize the effect of mobile ions in the $FASn_{0.5}Pb_{0.5}I_3$ samples with different SnF_2 concentrations, we perform hyperspectral PL imaging upon biasing lateral devices (Fig. 5a). We track the intensity changes of the PL peak (990 nm) as a function of time while applying a constant bias of 30 V. To discard any light-soaking effect from the excitation source, we initially track the PL without any bias (Fig. S17a, ESI†). While the excitation light does not produce substantial changes

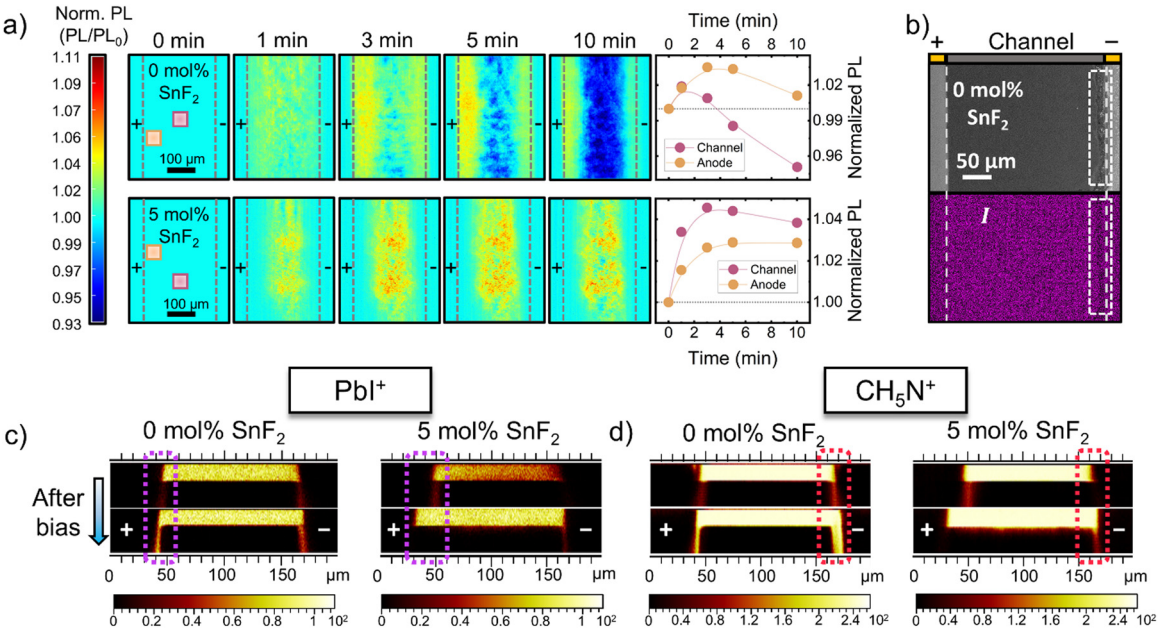

Fig. 5 (a) Hyperspectral PL maps from the Au/Cr/$FASn_{0.5}Pb_{0.5}I_3$ (channel length is 300 μm)/Cr/Au lateral devices upon 30 V bias, the SnF_2 concentrations are: 0 mol% and 5 mol%. We tracked the PL emission from mainly two areas: the channel and the anode, these are indicated by the pink and orange squares on the 0 min frames for each sample. Each frame was recorded every 1 minute. For clarity, we only displayed 5 frames per sample. The rest of the data set can be found in Fig. S10b (ESI†). (b) SEM images (top panel) and I EDS elemental maps (bottom panel) from the 0 mol% sample after 30 V bias for 1 hour. The white square highlights the damaged region after biasing. ToF-SIMS x–z depth profile maps of: (c) PbI^+ and (d) CH_5N^+ fragments from the 0 and 5 mol% SnF_2 samples before and after bias.

in PL in most of the samples, a more detailed comment on this is given in Note S6 (ESI†). In the first minute of biasing, the channel from the 0 mol% SnF_2 sample presents a 2% increase in the PL intensity. After 5 minutes, the emission reduces at the centre of the channel and a more intense signal appears near the positive electrode. During the following 10 minutes, the PL signal from the channel decreases 6% of the initial state, while the emission from the anode side increases 1%. PL quenching originates from the propagation of mobile ions towards the contacts, leaving behind an area with high defect density that enhances non-radiative recombination, as demonstrated by earlier reports.[24,60] Furthermore, the increase in PL intensity observed near the anode is consistent with the accumulation of mobile anionic species (*i.e.*, I^-) and the passivation of ionic vacancies in this region. The 5 mol% SnF_2 sample similarly reveals a slight increase of 4% in the emission upon biasing. After 3 min, the PL intensity remains almost unchanged for the duration of the measurement. The 2.5 and 10 mol% SnF_2 samples present a similar behaviour as the 5 mol%, sustaining a relatively constant PL emission during the biasing (Fig. S17b, ESI†). These opposing responses to the bias could be related to the higher n_{ion} found in the samples without SnF_2 (Fig. 3c). In this case, a higher density of defects is created since there are more mobile ions susceptible to the applied electric field, causing a faster reduction of the PL emission in the channel.

To confirm if ionic species are being mobilized by the applied electric field and their possible composition, we perform elemental mapping using energy-dispersive X-ray spectroscopy (EDS) and time-of-flight-secondary ion mass spectroscopy (ToF-SIMS). For both techniques, we track the changes of different species of interest before and after biasing the 0 mol% and 5 mol% SnF_2 samples at 30 V bias for 1 hour. After biasing, we notice an evident morphology change near the cathode region that is only present in the 0 mol% SnF_2 sample. The EDS mapping reveals a significant absence of iodine in the degraded region (Fig. 5b). Interestingly, we also observe a decrease of Sn in the damaged region (Fig. S18a, ESI†). The absence of I and Sn are consistent with the I^- migration-induced formation of I_2 and the subsequent degradation of the Sn–Pb perovskite (a more in-depth discussion is provided in Note S7, ESI†). In comparison, the 5 mol% film do not show significant variations in the I, Sn, and Pb content along the channel (Fig. S18b, ESI†). Furthermore, we employ ToF-SIMS depth profiling (3D chemical mapping) to elucidate variations in the distribution of the perovskite constituent secondary ions within the channel and under the electrodes. The process takes place *via* a non-interlaced depth profiling method employing alternating imaging and sputtering cycles (employing a 30 keV Bi_3^+ primary ion beam and a 20 keV Ar_{2000}^+ sputtering ion beam). The secondary ion images presented in Fig. 5c and d represent an x–z cross-section of the channel between the electrodes as well as the edges of the positive and negative electrodes. An illustration of a complete x–y, x–z and y–z series of ion images are shown for reference in Fig. S19 (ESI†). ToF-SIMS mapping from the 0 mol% samples show a higher concentration of PbI^+ near the anode vicinity after biasing (Fig. 5c). Other iodide-based fragments, such as $Pb_2I_3^+$, and SnI^+, display a similar behaviour (Fig. S20, ESI†), compatible

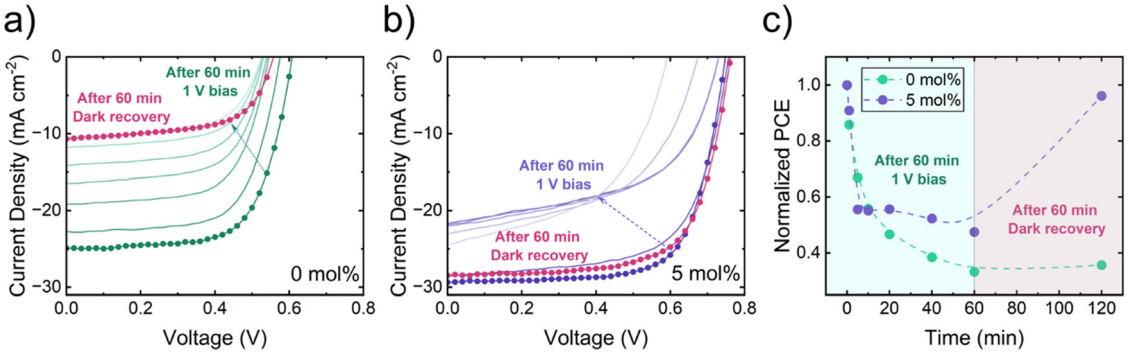

Fig. 6 *IV* curves from ITO/PEDOT:PSS/$Cs_{0.25}FA_{0.75}Sn_{0.5}Pb_{0.5}I_3$/$C_{60}$/BCP/Cu solar cells with (a) 0 mol% and (b) 5 mol% SnF_2 recorded during 1 V bias stressing for 60 min. After resting the devices for 60 min under dark, another *IV* is acquired. (c) Normalized PCE as a function of time from the 0 mol% and 5 mol% SnF_2 devices. The initial efficiencies are 10.1 and 15.5 for the devices with 0 and 5 mol%, respectively.

with mobile iodide migration. Interestingly, we further detect a higher concentration of CH_5N^+ fragments near the cathode area, consistent with an accumulation of FA^+ ions (Fig. 5d). In contrast, the accumulation of these species near the electrodes is not visible after biasing the 5 mol% samples (Fig. S21, ESI†). The vertical extensions of the PbI^+ and CH_5N^+ secondary ions at the outer edges of the channel represent material beneath the Au and Cr electrode regions which are revealed during depth profiling (this is illustrated using the Au_3^+ and Cr^+ secondary ions for an example system in Fig. S22, ESI†). Additionally, we examine the potential for F^- migration after the application of bias. The depth profile maps show an accumulation of F^- at the top and bottom surfaces, as shown in previous research.[61] However, we do not observe a preferential accumulation of F^- at either of the contacts, suggesting that F^- migration is an unlikely process (Fig. S23, ESI†). Based on these results, we identify that the migration of I^- and FA^+ in mixed Sn–Pb perovskites correlates well with a higher concentration of V_{Sn}^{2-} and h^+.

Implications of the mixed ionic-electronic conduction in the bias stability of Sn–Pb perovskite solar cells

Finally, we investigate the implications of these findings on the stability of Sn-based perovskites solar cells under continuous forward biasing. We monitor the power conversion efficiency (PCE) from *IV* curves of SnPb perovskite solar cells (ITO/PEDOT:PSS/$Cs_{0.25}FA_{0.75}Sn_{0.5}Pb_{0.5}I_3$/$C_{60}$/BCP/Cu) upon forward biasing at 1 V under dark (Fig. 6). We test the bias stability of the device with perovskite compositions containing 0 mol% and 5 mol% SnF_2 (the photovoltaic parameters of both devices are summarized in Fig. S24, ESI†). The aim of these experiments is to induce device failure by leveraging mechanisms primarily linked to ion migration, as other factors such as temperature or light result in more intricate degradation pathways. Importantly, several reports have shown that aging devices under forward biasing exhibits similar degradation dynamics compared to illumination and outdoor testing.[62–64] Effects such as charge collection losses, defect growth, degradation of crystalline structure and electrochemical reactions at the interfaces can be reproduced with forward bias tests. Consequently, results from bias-induced degradation could provide a preliminary understanding on the stability of photovoltaic devices when subjected to real-world conditions, including variations in temperature and light exposure.

From the analysis of all the photovoltaic parameters, we notice that the current density (J_{sc}) experiences the most significant losses in both 0 mol% and 5 mol% SnF_2 samples. The PCE from the device containing 0 mol% SnF_2 decays exponentially, reaching 33% of its initial efficiency after 60 min (Fig. 6a). The 5 mol% sample shows a rapid PCE decrease during the first 5 minutes of biasing, after which the PCE remains relatively stable at 44% of the original PCE for the rest of the biasing period (Fig. 6b). These fast performance losses are associated with an accumulation of ions at the interfaces with the contacts, inducing a severe screening of the built-in potential.[8,65] Notably, we detect a significant difference in the PCE after resting the devices for 1 hour under dark conditions. While the device with 0 mol% SnF_2 presents a permanent loss of performance after the resting period, the 5 mol% SnF_2 sample almost recovers to their initial efficiency (Fig. 6c). The irreversible degradation in the 0 mol% SnF_2 device agrees with the more severe ion migration and the I and Sn loss recorded in our EDS experiments (Fig. 5b). The increase of n_{ion} and the concentration of V_{Sn}^{2-} in the samples without SnF_2 could favor detrimental chemical reactions with the transport layers or within the perovskite, resulting in a permanent degradation at the interfaces or the perovskite bulk (a more detailed discussion on the possible degradation mechanism under bias stress is provided in Note S8, ESI†). Therefore, these results demonstrate that efficiency losses attributed to bias stress in SnPb perovskites are considerable and are correlated to the mixed ion-electronic properties of these materials.

Conclusions

In summary, we investigate the mixed ionic-electronic transport properties of Sn-based perovskites and find that the σ_{elec} and σ_{ion} undergo a simultaneous increase at higher Sn fractions. Our experimental results indicate that this behaviour is due to an enhancement in $[p]$ and V_{Sn}^{2-}, which is followed by a

rise in n_{ion} and prominent lateral ion migration. This implies that the strong p-doping in Sn-based perovskites not only modulates the σ_{elec} but also the σ_{ion}. First-principles simulations reveal that the combined effect of h^+ and V_{Sn}^{2-} facilitate I^- migration. The excess of positively charged h^+ near the vicinity of a V_{Sn}^{2-} promotes the movement of the negatively charged I^- through attractive electrostatic interactions, thereby reducing the migration barrier for I^- migration. We verify these insights through elemental mapping, where we identify that I^- and FA^+ migration exacerbates at a higher concentration of V_{Sn}^{2-} and h^+. Overall, these results highlight the combined effect of vacancies and electronic carriers on the ion transport in Sn-based perovskites. Considering the tendency of these materials for self p-doping, we demonstrate that the relation between V_{Sn}^{2-}, h^+, and mobile ions has major implications for the bias stability of Sn-based perovskite solar cells. Hence, the detailed picture of the mixed ionic-electronic transport in Sn-based perovskites provided herein is of great relevance towards high performing and stable Sn-based perovskite technologies.

Experimental section

Materials

CsI (dry beads 99.999%), PbI_2 (dry beads, 99.999%), SnI_2 (99.99%), SnF_2, bathocuproine (BCP), DMSO, DMF, and chlorobenzene (all anhydrous) were obtained from Sigma Aldrich. MAI, FAI, and MACl were provided by Greatcell. Cr (99.95%), Au (99.99%), and Cu (99.9%) pellets were purchased from Kurt J. Lesker. C_{60} was supplied by nanoC. PEDOT:PSS AI 4083 was obtained from Heraeus.

Perovskite solution preparation

All the perovskite solutions were prepared by weighting the respective precursor salts (CsI, MAI, MACl, FAI PbI_2, SnI_2, and SnF_2, with their ratios corresponding to the stoichiometry of the desired composition) in a single glass vial. MACl was added for the $FAPbI_3$ composition to stabilize the α-phase while only leaving traces of MA, the concentration of MACl used was 32 mg ml^{-1}.[66] For the galvanostatic polarization measurements from the MA, FA, and CsFA series, the concentration of SnF_2 was set to 10 mol% with respect to the concentration of SnI_2 of each composition. The precursors were dissolved in a mixture of DMF:DMSO and stirred for 1 hour before using the solution. The DMF : DMSO ratio varied depending on the composition, for pure Pb compositions a 4 : 1 ratio was used, for the rest of the compositions a 3 : 1 ratio was selected. The concentration of all the solutions used to prepare the samples for the galvanostatic polarization, hyperspectral PL, and capacitance voltage measurements was set to 1.2 M. For the fabrication of the perovskite solar cell, a 1.6 M solution was prepared. All solutions were stirred for 1 h. Solution preparation was carried inside a N_2 glovebox with trace levels of O_2 (< 0.1 ppm).

Film characterization

SEM images were taken with a Zeiss Auriga microscope operated at 5 keV. X-Ray diffraction patterns were acquired with a Bruker D8 advanced diffractometer employing Cu-K_α radiation. SEM-EDS based experiment were performed in Thermo Scientific™ (FEI) DualBeam SEM-FIB Helios G5 operated at 10 keV, and equipped with UltraDry EDS Detector with 129 eV energy resolution. Additionally, some SEM images were taken with a Zeiss Auriga microscope (5 keV). X-Ray diffraction (XRD) patterns were acquired with a Bruker D8 advanced diffractometer employing Cu-Kα radiation.

ToF-SIMS elemental analysis

Analysis was conducted using a HybridSIMS instrument (ION-TOF, GmbH). Dual-beam dynamic SIMS was conducted using a 20 keV Ar_{2000} gas cluster ion beam (GCIB) with a target current of 1 nA as a sputter beam and 30 keV Bi^{3+} analysis beam with a pulsed target current of ~0.03 pA. Non-interlaced depth profiling was employed, whereby the sputter and analysis ion beams operate at alternating intervals with 5 frames of sputtering per 5 analysis frame and a 0.5 s pause between the sputtering and analysis. A region of 350 μm × 350 μm was sputtered, and a 200 μm × 200 μm region was analyzed with pixel density 256 × 256. The data was collected in positive polarity for 393 seconds. The biased samples were subjected to an electric field of 27 V for 1 hour inside a N_2 glovebox.

Sample preparation for galvanostatic polarization and hyperspectral PL measurements

Glass substrates (Xinyan Technology, 2.5 × 2.5 cm^2) were sequentially sonicated in a Hellmanex aqueous solution, deionized water, acetone, and isopropanol for 10 min each. Substrates were dried with N_2 and treated with UV ozone for 15 min. A two-step spin-coating procedure of 1000 rpm for 10 s and 4000 rpm for 40 s was used for the deposition of the perovskite films. Chlorobenzene (100 μl) is used as antisolvent in all compositions, the timing at which CB is added varied according to the composition. After the antisolvent quenching, most compositions were annealed at 100 °C for 10 min except for the $MAPbI_3$, and $FAPbI_3$ sample, which were annealed at 100 and 150 °C for 30 and 10 min, respectively. The perovskite deposition was followed by the sequential thermal evaporation of Cr (10 nm) and Au (60 nm), this was carried under high vacuum by an Angstrom Engineering system. All processing was performed inside a N_2 glovebox with O_2 levels below 0.1 ppm and continuous purging.

Sample preparation for the capacitance–voltage measurements and solar cell fabrication

Pre-patterned ITO/glass substrates (Xinyan Technology, 10/15 Ω sq^{-1}, CN) were sequentially sonicated in a Hellmanex aqueous solution, deionized water, acetone, and isopropanol for 10 min each. Substrates were dried with N_2 and treated with UV ozone for 15 min. A solution of PEDOT : PSS and isopropanol (1 : 1) was coated on the clean ITO at 4000 rpm for 50 s, then annealed at 150 °C for 10 min. Then, samples were transferred immediately to a N_2 glovebox with O_2 levels below 0.1 ppm. A two-step spin-coating procedure of 1000 rpm for 10 s and 4000 rpm for 40 s was used for the deposition of the perovskite films. CB was added at the 15th s of the second step. Samples with the

compositions $FASn_{0.5}Pb_{0.5}I_3$ and $Cs_{0.25}FA_{0.75}Sn_{0.5}Pb_{0.5}I_3$ are annealed at 100 °C and 120 °C for 10 min, respectively. Subsequently, C_{60} (30 nm) and BCP (7 nm) were thermally evaporated at a rate of 0.1 A s^{-1} under high vacuum by using an Angstrom Engineering system. Finally, 100 nm of Cu stripes were thermally evaporated to result in devices with an area of 0.1 cm^2.

Galvanostatic polarization measurements

Samples were transfer from inside the glovebox to a Nextron chamber with a 2 probe configuration, with ultra-pure N_2 (99.999%) being continuously injected to the chamber. The temperature of the sample was actively fixed to 40 °C with a Peltier module controlled by the software provided by the company. Before the measurement started, a waiting time of 10 min was given to stabilize the temperature of the sample. The electrical measurements were performed with a Keithley 4200 semiconductor parameter analyzer. The injected current was selected to produce low voltages of ~100 mV. At such voltages, we reduce the risk of any irreversible reaction (in the perovskite bulk or the perovskite/contacts interface) that could be induced by the constant flow of current. The σ_{tot} is calculated from the following equation: $\sigma_{tot} = \frac{I}{V_{t\approx 0}} \cdot \frac{L}{dw}$, where I is the applied current, $V_{t=0}$ is the voltage measured at the initial point in time (t), L is the channel length (150 μm), d is the thickness of the perovskite (~300 nm), and w is the width of the electrode (3 μm). The σ_{elec} is estimated from the following equation: $\sigma_{elec} = \frac{I}{V_{t\approx a}} \cdot \frac{L}{dw}$, where $V_{t=a}$ is the voltage after some time a, which was characterized by the stabilization of the voltage. The stabilization time varied according to the composition, but it was typically observed in the range of 10^2 seconds. The σ_{ion} was deduced from the equation: $\sigma_{ion} = \sigma_{elec} - \sigma_{tot}$.

Capacitance–voltage measurements

The capacitance–voltage measurements were performed with a Fluxim Paios characterization suite inside a N_2 glovebox. The AC frequency for the low frequency measurements was set to 4 Hz with an amplitude of 20 mV. The measurement was executed in a voltage range from −0.2 to 0.3 V with scan speed of 0.7 V s^{-1}. The n_{ion} was extracted from the linear region of this range by the following formula: $\frac{d(C_{depl}^{-2})}{dV_{app}} = -\frac{2}{n_{ion} q \varepsilon \varepsilon_0}$.[57] The value of ε = 37 was extracted from the geometrical capacitance obtained from capacitance *vs.* frequency plots (Fig. S14, ESI†). The relative permittivity is deduced from the geometrical capacitance (the capacitance at 10 kHz) with the following relation: $C_{geo} = \frac{\varepsilon \varepsilon_0}{d}$.[54] For the high frequency measurements, an AC signal of 10 kHz with an amplitude of 10 mV was selected. The chosen voltage range was from −0.2 to 0.8 with a scan rate of 0.7 V s^{-1}. The p was estimated from the Mott Schottky analysis given by: $\frac{1}{C^2} = \frac{2(V_{bi} - V)}{q \varepsilon \varepsilon_0 p}$, where V_{bi} is the built-in voltage. All measurements are taken under N_2 and dark conditions.

BACE measurements

In dark BACE, the device was initially held at a voltage close to the open-circuit voltage in the dark, where the injected charge equals the short-circuit current. After a pre-set delay time, a bias of 0 V was applied to extract the injected and capacitive charge in the device. The delay times for the fresh devices were chosen to be typically five times longer than the extraction time of charges observed under the collection bias (typically ~5–10 s) to allow ionic charges to distribute throughout the active layer. The extracted charge was obtained by integrating the current transient and the charge carrier density by dividing the total charge by the elementary charge and the cell volume. The measurements were performed using the ion characterization system from FastChar UG.

Hyperspectral PL measurements

Hyperspectral PL imaging was carried out with a IMA hyperspectral microscopy system (photon *etc*). A bias of 30 V was applied to samples in the dark during every time step, after which bias was stopped and PL was acquiered by exciting the sample with a continuous-wave 405 nm laser. PL images where then normalized to t = 0 min to visualize changes in PL induced by ion migration. Samples were encapsulated with a glass slide and a polyurethane sealant.

Solar cell characterization

A Xe arc lamp solar simulator (ABET Sun 2000, class A) calibrated to ±5% of AM1.5G between 350–1100 nm was used to obtain current–voltage curves. To record the *J–V* response, a Keithley 2400-series source-measure unit was used with a scan speed of 0.15 V s^{-1}. For the stability measurements, a *J–V* was recorded for specific times while devices were under 1 V forwards bias. For the entire duration of the measurement, devices were kept under a N2 glovebox (<0.1 ppm).

DFT calculations

First-principles calculations were employed using density functional theory (DFT) based on plane-wave basis set and the projected augmented wave method, as implemented in the VASP package.[67,68] SCAN+rvv10 type meta-GGA with vdW functional was used to describe the exchange–correlation functionals.[69,70] All starting geometries are generated based on the experimental lattice parameters of $FAPbI_3$. A cut-off energy of 400 eV for the plane-wave basis sets and 4 × 4 × 4 for gamma-centered *k*-mesh are used for the self-consistent field calculations and geometry optimizations. In geometry optimizations, the ionic positions and cell dimensions were allowed to relax, using a conjugate gradient algorithm, until all residual forces are smaller than 0.02 eV $Å^{-1}$.

Migration barriers were determined from the energy profiles of iodine migration along the reaction path from one site towards the nearest iodine-vacancy defect. The initial and final structures were relaxed first, followed by a linear interpolation scheme to generate intermediate structures along the migration pathway. The energy profiles were calculated using the nudged

elastic band and constrained energy minimization methods. 16 grid points were considered for energy profile calculations. The energy barriers associated with the iodide migrations were determined from the energy difference between the minimum energy and the saddle point.

Author contributions

L. H. H fabricated all the samples, measured XRD and SEM, and performed the galvanostatic polarization, capacitance–voltage, and solar cells characterization measurements. L. L. assisted with sample preparation and the hyperspectral PL measurements. A M. K., M. P., D. J. S. conducted the ToF-SIMS measurements. I. Y. performed the DFT calculations. N. K. and M. S. performed the BACE characterizations. B. V. and S. W. assisted with SEM and EDS measurements. M. G. R. participated in the development of the experimental set-ups. L. H. H., L. L., and D. B. conceived the idea, directed the project, and wrote the manuscript. All authors read and commented on the manuscript.

Data availability

The data supporting the article have been included as part of the ESI.†

Conflicts of interest

The authors declare no competing interests.

Acknowledgements

Part of the research reported in this publication was supported by funding from King Abdullah University of Science and Technology (KAUST) - Center of Excellence for Renewable Energy and Storage Technologies, under award number 5937. All authors thank the KAUST Solar Platform (KSP) for granting access to the characterization and device fabrication facilities and equipment employed herein. M. S. acknowledges the Vice-Chancellor Early Career Professorship Scheme from CUHK for funding.

References

1 B. A. Rosales, K. Schutt, J. J. Berry and L. M. Wheeler, *ACS Energy Lett.*, 2023, **8**, 1705–1715.
2 C. Eames, J. M. Frost, P. R. F. Barnes, B. C. O'Regan, A. Walsh and M. S. Islam, *Nat. Commun.*, 2015, **6**, 7497.
3 E. Mosconi and F. De Angelis, *ACS Energy Lett.*, 2016, **1**, 182–188.
4 T.-Y. Yang, G. Gregori, N. Pellet, M. Grätzel and J. Maier, *Angew. Chem., Int. Ed.*, 2015, **54**, 7905–7910.
5 G. Y. Kim, A. Senocrate, Y.-R. Wang, D. Moia and J. Maier, *Angew. Chem., Int. Ed.*, 2021, **60**, 820–826.
6 R. A. Kerner and B. P. Rand, *J. Phys. Chem. Lett.*, 2018, **9**, 132–137.
7 P. Calado, A. M. Telford, D. Bryant, X. Li, J. Nelson, B. C. O'Regan and P. R. F. Barnes, *Nat. Commun.*, 2016, **7**, 13831.
8 J. Thiesbrummel, V. M. Le Corre, F. Peña-Camargo, L. Perdigón-Toro, F. Lang, F. Yang, M. Grischek, E. Gutierrez-Partida, J. Warby, M. D. Farrar, S. Mahesh, P. Caprioglio, S. Albrecht, D. Neher, H. J. Snaith and M. Stolterfoht, *Adv. Energy Mater.*, 2021, **11**, 2101447.
9 V. M. Le Corre, J. Diekmann, F. Peña-Camargo, J. Thiesbrummel, N. Tokmoldin, E. Gutierrez-Partida, K. P. Peters, L. Perdigón-Toro, M. H. Futscher, F. Lang, J. Warby, H. J. Snaith, D. Neher and M. Stolterfoht, *Sol. RRL*, 2022, **6**, 2100772.
10 J. Carrillo, A. Guerrero, S. Rahimnejad, O. Almora, I. Zarazua, E. Mas-Marza, J. Bisquert and G. Garcia-Belmonte, *Adv. Energy Mater.*, 2016, **6**, 1502246.
11 D. Lin, T. Shi, H. Xie, F. Wan, X. Ren, K. Liu, Y. Zhao, L. Ke, Y. Lin, Y. Gao, X. Xu, W. Xie, P. Liu and Y. Yuan, *Adv. Energy Mater.*, 2021, **11**, 2002552.
12 D. Moia, I. Gelmetti, P. Calado, W. Fisher, M. Stringer, O. Game, Y. Hu, P. Docampo, D. Lidzey, E. Palomares, J. Nelson and P. R. F. Barnes, *Energy Environ. Sci.*, 2019, **12**, 1296–1308.
13 S. Reichert, Q. An, Y.-W. Woo, A. Walsh, Y. Vaynzof and C. Deibel, *Nat. Commun.*, 2020, **11**, 6098.
14 M. A. Haque, L. H. Hernandez, B. Davaasuren, D. R. Villalva, J. Troughton and D. Baran, *Adv. Energy Sustainability Res.*, 2020, **1**, 2000033.
15 T. Liu, X. Zhao, J. Li, Z. Liu, F. Liscio, S. Milita, B. C. Schroeder and O. Fenwick, *Nat. Commun.*, 2019, **10**, 5750.
16 R. Tounesi, L. H. Hernandez, L. Lanzetta, S. Jang, B. Davaasuren, M. A. Haque and D. Baran, *ACS Appl. Electron. Mater.*, 2023, **6**, 2826–2831.
17 D. Meggiolaro, D. Ricciarelli, A. A. Alasmari, F. A. S. Alasmary and F. De Angelis, *J. Phys. Chem. Lett.*, 2020, **11**, 3546–3556.
18 L. Lanzetta, T. Webb, J. M. Marin-Beloqui, T. J. Macdonald and S. A. Haque, *Angew. Chem., Int. Ed.*, 2023, **62**, e202213966.
19 M. A. Haque, T. Zhu, L. H. Hernandez, R. Tounesi, C. Combe, B. Davaasuren, A.-H. Emwas, F. P. García de Arquer, E. H. Sargent and D. Baran, *Cell Rep. Phys. Sci.*, 2023, **4**, 101703.
20 L. Lanzetta, L. Gregori, L. H. Hernandez, A. Sharma, S. Kern, A. M. Kotowska, A.-H. Emwas, L. Gutiérrez-Arzaluz, D. J. Scurr, M. Piggott, D. Meggiolaro, M. A. Haque, F. De Angelis and D. Baran, *ACS Energy Lett.*, 2023, **8**, 2858–2867.
21 N. Li, Z. Zhu, J. Li, A. K.-Y. Jen and L. Wang, *Adv. Energy Mater.*, 2018, **8**, 1800525.
22 K. O. Ighodalo, W. Chen, Z. Liang, Y. Shi, S. Chu, Y. Zhang, R. Khan, H. Zhou, X. Pan, J. Ye and Z. Xiao, *Angew. Chem., Int. Ed.*, 2023, **62**, e202213932.
23 S. Martani, Y. Zhou, I. Poli, E. Aktas, D. Meggiolaro, J. Jiménez-López, E. L. Wong, L. Gregori, M. Prato, D. Di Girolamo, A. Abate, F. De Angelis and A. Petrozza, *ACS Energy Lett.*, 2023, **8**, 2801–2808.

24 S. P. Senanayak, K. Dey, R. Shivanna, W. Li, D. Ghosh, Y. Zhang, B. Roose, S. J. Zelewski, Z. Andaji-Garmaroudi, W. Wood, N. Tiwale, J. L. MacManus-Driscoll, R. H. Friend, S. D. Stranks and H. Sirringhaus, *Nat. Mater.*, 2023, **22**, 216–224.
25 K. Dey, D. Ghosh, M. Pilot, S. R. Pering, B. Roose, P. Deswal, S. P. Senanayak, P. J. Cameron, M. S. Islam and S. D. Stranks, *Energy Environ. Sci.*, 2024, **17**, 760–769.
26 C. Li, Z. Song, C. Chen, C. Xiao, B. Subedi, S. P. Harvey, N. Shrestha, K. K. Subedi, L. Chen, D. Liu, Y. Li, Y.-W. Kim, C.-S. Jiang, M. J. Heben, D. Zhao, R. J. Ellingson, N. J. Podraza, M. Al-Jassim and Y. Yan, *Nat. Energy*, 2020, **5**, 768–776.
27 J. Thiesbrummel, S. Shah, E. Gutierrez-Partida, F. Zu, F. Peña-Camargo, S. Zeiske, J. Diekmann, F. Ye, K. P. Peters, K. O. Brinkmann, P. Caprioglio, A. Dasgupta, S. Seo, F. A. Adeleye, J. Warby, Q. Jeangros, F. Lang, S. Zhang, S. Albrecht, T. Riedl, A. Armin, D. Neher, N. Koch, Y. Wu, V. M. Le Corre, H. Snaith and M. Stolterfoht, *Nat. Energy*, 2024, **9**, 664–676.
28 J. Wang, M. A. Uddin, B. Chen, X. Ying, Z. Ni, Y. Zhou, M. Li, M. Wang, Z. Yu and J. Huang, *Adv. Energy Mater.*, 2023, **13**, 2204115.
29 J. Sanchez-Diaz, R. S. Sánchez, S. Masi, M. Krečmarová, A. O. Alvarez, E. M. Barea, J. Rodriguez-Romero, V. S. Chirvony, J. F. Sánchez-Royo, J. P. Martinez-Pastor and I. Mora-Seró, *Joule*, 2022, **6**, 861–883.
30 L. Lanzetta, T. Webb, N. Zibouche, X. Liang, D. Ding, G. Min, R. J. E. Westbrook, B. Gaggio, T. J. Macdonald, M. S. Islam and S. A. Haque, *Nat. Commun.*, 2021, **12**, 2853.
31 A. Alsulami, L. Lanzetta, L. Huerta Hernandez, D. Rosas Villalva, A. Sharma, S. P. Gonzalez Lopez, A.-H. Emwas, A. Yazmaciyan, F. Laquai, I. Yavuz and D. Baran, *J. Am. Chem. Soc.*, 2024, **146**, 22970–22981.
32 S. Gupta, D. Cahen and G. Hodes, *J. Phys. Chem. C*, 2018, **122**, 13926–13936.
33 G. Y. Kim, A. Senocrate, T.-Y. Yang, G. Gregori, M. Grätzel and J. Maier, *Nat. Mater.*, 2018, **17**, 445–449.
34 A. Senocrate, I. Moudrakovski, G. Y. Kim, T.-Y. Yang, G. Gregori, M. Grätzel and J. Maier, *Angew. Chem., Int. Ed.*, 2017, **56**, 7755–7759.
35 A. Senocrate, I. Spanopoulos, N. Zibouche, J. Maier, M. S. Islam and M. G. Kanatzidis, *Chem. Mater.*, 2021, **33**, 719–726.
36 F. Peña-Camargo, J. Thiesbrummel, H. Hempel, A. Musiienko, V. M. Le Corre, J. Diekmann, J. Warby, T. Unold, F. Lang, D. Neher and M. Stolterfoht, *Appl. Phys. Rev.*, 2022, **9**, 021409.
37 M. García-Batlle, S. Deumel, J. E. Huerdler, S. F. Tedde, A. Guerrero, O. Almora and G. Garcia-Belmonte, *ACS Appl. Mater. Interfaces*, 2021, **13**, 35617–35624.
38 J. Zhao, Y. Deng, H. Wei, X. Zheng, Z. Yu, Y. Shao, J. E. Shield and J. Huang, *Sci. Adv.*, 2017, **3**, eaao5616.
39 L. McGovern, I. Koschany, G. Grimaldi, L. A. Muscarella and B. Ehrler, *J. Phys. Chem. Lett.*, 2021, **12**, 2423–2428.
40 M. Ghasemi, B. Guo, K. Darabi, T. Wang, K. Wang, C.-W. Huang, B. M. Lefler, L. Taussig, M. Chauhan, G. Baucom, T. Kim, E. D. Gomez, J. M. Atkin, S. Priya and A. Amassian, *Nat. Mater.*, 2023, **22**, 329–337.
41 Y. Shao, Y. Fang, T. Li, Q. Wang, Q. Dong, Y. Deng, Y. Yuan, H. Wei, M. Wang, A. Gruverman, J. Shield and J. Huang, *Energy Environ. Sci.*, 2016, **9**, 1752–1759.
42 F. Hao, C. C. Stoumpos, P. Guo, N. Zhou, T. J. Marks, R. P. H. Chang and M. G. Kanatzidis, *J. Am. Chem. Soc.*, 2015, **137**, 11445–11452.
43 G. Nasti, M. H. Aldamasy, M. A. Flatken, P. Musto, P. Matczak, A. Dallmann, A. Hoell, A. Musiienko, H. Hempel, E. Aktas, D. Di Girolamo, J. Pascual, G. Li, M. Li, L. V. Mercaldo, P. D. Veneri and A. Abate, *ACS Energy Lett.*, 2022, **7**, 3197–3203.
44 S. Kahmann, Z. Chen, O. Hordiichuk, O. Nazarenko, S. Shao, M. V. Kovalenko, G. R. Blake, S. Tao and M. A. Loi, *ACS Appl. Mater. Interfaces*, 2022, **14**, 34253–34261.
45 D. Kim, J. S. Yun, P. Sharma, D. S. Lee, J. Kim, A. M. Soufiani, S. Huang, M. A. Green, A. W. Y. Ho-Baillie and J. Seidel, *Nat. Commun.*, 2019, **10**, 444.
46 K. Nishimura, D. Hirotani, M. A. Kamarudin, Q. Shen, T. Toyoda, S. Iikubo, T. Minemoto, K. Yoshino and S. Hayase, *ACS Appl. Mater. Interfaces*, 2019, **11**, 31105–31110.
47 T. J. Macdonald, L. Lanzetta, X. Liang, D. Ding and S. A. Haque, *Adv. Mater.*, 2023, **35**, 2206684.
48 M. Pitaro, E. K. Tekelenburg, S. Shao and M. A. Loi, *Adv. Mater.*, 2022, **34**, 2105844.
49 M. H. Kumar, S. Dharani, W. L. Leong, P. P. Boix, R. R. Prabhakar, T. Baikie, C. Shi, H. Ding, R. Ramesh, M. Asta, M. Graetzel, S. G. Mhaisalkar and N. Mathews, *Adv. Mater.*, 2014, **26**, 7122–7127.
50 K. J. Savill, A. M. Ulatowski, M. D. Farrar, M. B. Johnston, H. J. Snaith and L. M. Herz, *Adv. Funct. Mater.*, 2020, **30**, 2005594.
51 J. Pascual, M. Flatken, R. Félix, G. Li, S.-H. Turren-Cruz, M. H. Aldamasy, C. Hartmann, M. Li, D. Di Girolamo, G. Nasti, E. Hüsam, R. G. Wilks, A. Dallmann, M. Bär, A. Hoell and A. Abate, *Angew. Chem., Int. Ed.*, 2021, **60**, 21583–21591.
52 Q. Chen, J. Luo, R. He, H. Lai, S. Ren, Y. Jiang, Z. Wan, W. Wang, X. Hao, Y. Wang, J. Zhang, I. Constantinou, C. Wang, L. Wu, F. Fu and D. Zhao, *Adv. Energy Mater.*, 2021, **11**, 2101045.
53 H. Lee, S. Gaiaschi, P. Chapon, D. Tondelier, J.-E. Bourée, Y. Bonnassieux, V. Derycke and B. Geffroy, *J. Phys. Chem. C*, 2019, **123**, 17728–17734.
54 O. Almora, C. Aranda, E. Mas-Marzá and G. Garcia-Belmonte, *Appl. Phys. Lett.*, 2016, **109**, 173903.
55 S. Ravishankar, Z. Liu, U. Rau and T. Kirchartz, *PRX Energy*, 2022, **1**, 013003.
56 J. Tong, Q. Jiang, A. J. Ferguson, A. F. Palmstrom, X. Wang, J. Hao, S. P. Dunfield, A. E. Louks, S. P. Harvey, C. Li, H. Lu, R. M. France, S. A. Johnson, F. Zhang, M. Yang, J. F. Geisz, M. D. McGehee, M. C. Beard, Y. Yan, D. Kuciauskas, J. J. Berry and K. Zhu, *Nat. Energy*, 2022, 642–651.
57 J. Diekmann, F. Peña-Camargo, N. Tokmoldin, J. Thiesbrummel, J. Warby, E. Gutierrez-Partida, S. Shah, D. Neher and M. Stolterfoht, *J. Phys. Chem. Lett.*, 2023, **14**, 4200–4210.

58 Y. Zhao, I. Yavuz, M. Wang, M. H. Weber, M. Xu, J.-H. Lee, S. Tan, T. Huang, D. Meng, R. Wang, J. Xue, S.-J. Lee, S.-H. Bae, A. Zhang, S.-G. Choi, Y. Yin, J. Liu, T.-H. Han, Y. Shi, H. Ma, W. Yang, Q. Xing, Y. Zhou, P. Shi, S. Wang, E. Zhang, J. Bian, X. Pan, N.-G. Park, J.-W. Lee and Y. Yang, *Nat. Mater.*, 2022, **21**, 1396–1402.

59 M. Y. Toriyama, M. K. Brod and G. J. Snyder, *ChemNanoMat*, 2022, **8**, e202200222.

60 C. Li, A. Guerrero, S. Huettner and J. Bisquert, *Nat. Commun.*, 2018, **9**, 5113.

61 K. P. Marshall, M. Walker, R. I. Walton and R. A. Hatton, *Nat. Energy*, 2016, **1**, 16178.

62 U. Erdil, M. Khenkin, M. Remec, Q. Emery, V. Sudhakar, R. Schlatmann, A. Abate, E. A. Katz and C. Ulbrich, *ACS Energy Lett.*, 2025, **10**, 1529–1537.

63 M. A. Torre Cachafeiro, E. L. Comi, S. Parayil Shaji, S. Narbey, S. Jenatsch, E. Knapp and W. Tress, *Adv. Energy Mater.*, 2024, **15**, 2403850.

64 D. Di Girolamo, N. Phung, F. U. Kosasih, F. Di Giacomo, F. Matteocci, J. A. Smith, M. A. Flatken, H. Köbler, S. H. Turren Cruz, A. Mattoni, L. Cinà, B. Rech, A. Latini, G. Divitini, C. Ducati, A. Di Carlo, D. Dini and A. Abate, *Adv. Energy Mater.*, 2020, **10**, 2000310.

65 L. Huerta Hernandez, M. A. Haque, A. Sharma, L. Lanzetta, J. Bertrandie, A. Yazmaciyan, J. Troughton and D. Baran, *Sustainable Energy Fuels*, 2022, **6**, 4605–4613.

66 T. Zhu, D. Zheng, M.-N. Rager and T. Pauporté, *Sol. RRL*, 2020, **4**, 2000348.

67 G. Kresse and J. Hafner, *Phys. Rev. B:Condens. Matter Mater. Phys.*, 1993, **47**, 558–561.

68 G. Kresse and J. Furthmüller, *Comput. Mater. Sci.*, 1996, **6**, 15–50.

69 J. Klimeš, D. R. Bowler and A. Michaelides, *Phys. Rev. B:Condens. Matter Mater. Phys.*, 2011, **83**, 195131.

70 H. Peng, Z.-H. Yang, J. P. Perdew and J. Sun, *Phys. Rev. X*, 2016, **6**, 041005.